

Jesus Alvarez, Luis Diaz Angulo, Amelia Rubio Bretones,
Carlos M. de Jong van Coevorden, and Salvador G. Garcia

Efficient Antenna Modeling by DGTD

Leap-frog discontinuous Galerkin time-domain method.

An essential characteristic for the accurate simulation of wideband antenna systems is the modeling of their intricate geometrical details, including the feeding ports. In this article, we describe a leap-frog (LF) discontinuous Galerkin (DG) time-domain (TD) method combined with an efficient local time-stepping (LTS) strategy to deal with the high contrast in the element sizes for the electromagnetic modeling of these kinds of structures. The traditional delta-gap source model and a realistic coaxial port model are revisited. Numerical examples are presented and validated with measurements and commercial software simulations to demonstrate the applicability of the proposed approach.

METHODS USED FOR MODELING AND THEIR APPLICABILITY

Wideband antennas are key components in many different applications such as short-range and indoor ultrawideband communication systems, sensors for electronic countermeasure, and high-performance radar military systems. In these kinds of structures, an accurate modeling is critical in zones with small geometrical details, such as feeding ports. Frequency-domain (FD) methods, such as the method of moments and the finite-element method (FEM), are the usual choices for their ability to accurately model fine geometrical details. How-

ever, FD methods may become computationally inefficient for ultrawideband analysis since each frequency needs a complete simulation, typically involving a linear system resolution. TD methods are a natural alternative for these purposes. Advances in the TD formulations of FEMs have been made [1], but they still remain unaffordable for electrically large problems, such as those also requiring the

modeling of the antenna's surroundings (e.g., for onboard antennas), which has a strong influence on the antenna performance. Therefore, differential-based methods, such as the finite-difference TD (FDTD) and transmission-line-matrix method, are the usual choices in TD because of their computational simplicity. However, they all require some cube-based space partitioning, which imposes significant constraints on the geometrical discretization of complex objects that have arbitrary curvatures and intricate details. Techniques such as adaptive mesh refinement [2] and partially filled cells [3] exist to address this issue.

Recently, DG formulations of FEM have enabled affordable TD solvers (DGTD) to be built [4], [5]. These have most of the advantages of FDTD: spatially explicit algorithm, simplicity, easy parallelization, memory, and computational cost only growing linearly with the number of elements. At the same time, DGTD methods retain most of the benefits of FEM, specifically, adaptability of the unstructured meshes and spatial high-order convergence, thus enabling us to deal with problems where the required precision varies over the entire domain or when the solution lacks smoothness. In some cases, these methods have been applied to specific or canonical antenna problems for validation [6] and also for the analysis of wideband antennas with complex features [7]. In this article, the practical applicability of the method in terms of excitation, setup of the simulation, and truncation of the computational domain is described in detail based on real and complex antenna problems.

Two explicit time-integration schemes are commonly found in the DGTD literature: fourth-order Runge–Kutta (RK4) [4], [6] and second-order LF [8]. Both are conditionally stable and impose an upper bound for the maximum time step [9]. When DGTD is applied to antennas with small geometrical details, such as the feeding port, strong disparities among elements are found in the unstructured mesh and, hence, in the local time steps required for stability. This leads to a global time step constrained by the smallest one to ensure global stability and to a major waste of computational time in updating elements at a rate much higher than its own maximum time step. To avoid this problem, LTS strategies are employed [9]–[11].

Several alternatives have been proposed to find efficient DG schemes exploiting the versatility of the DG technique. Some of them are the use of different mesh elements, such as tetrahedral or hexahedral [12] or even hybrid meshes connected with pyramidal elements [13]. Another efficient technique to locally refine the mesh is the introduction of hanging nodes, resulting in nonconforming DG schemes [14], [15]. The schemes aimed to obtain hp-adaptability in the TD [16]–[18], where the use of high-order time integrators must be considered, deserve a special mention.

In this article, we present a new LTS scheme inspired by [9] for a second-order LF DGTD method (LFDG), and we demonstrate its applicability to the accurate simulation of wideband antennas. We revisit the basics of this method in the context of antenna simulation, paying special attention to the feed modeling. We analyze the classical delta-gap model and a realistic coaxial-port model whose excitation and truncation are easily accomplished in DGTD through the flux terms. Several examples serve to validate and show the accuracy and affordability of this approach for real antenna problems.

LFDG FORMULATION

The DGTD method is based on a geometrical discretization of the space into M nonoverlapping elements V^m , where we define element by element a local continuous basis of vector test functions ($\mathcal{B}^m = \{\Phi_1^m, \Phi_2^m, \dots, \Phi_Q^m\}$) and enforce the residue of Maxwell's curl equations to be orthogonal to each basis function. For instance, for source-free lossless linear isotropic homogeneous media

$$\langle \Phi_{q'}^m, \varepsilon \partial_t \mathbf{E}^m - \nabla \times \mathbf{H}^m \rangle_{V^m} = 0 \quad (1)$$

$$\langle \Phi_{q'}^m, \mu \partial_t \mathbf{H}^m + \nabla \times \mathbf{E}^m \rangle_{V^m} = 0 \quad \forall q' = (1, \dots, Q), m = (1, \dots, M), \quad (2)$$

where \mathbf{E} , \mathbf{H} , ε , μ , and m are the electric and magnetic field strength in Cartesian coordinates, permittivity, and permeability, respectively. After some algebraic computations, we can write (1) as

$$\int_{V^m} (\Phi_q^m \cdot (\epsilon \partial_t \mathbf{E}^m + \nabla \times \Phi_q^m \cdot \mathbf{H}^m)) dV = \oint_{\partial V^m} \Phi_q^m \cdot (\hat{\mathbf{n}}^m \times \mathbf{H}^m) dS \quad (3)$$

and similarly (2). The volume integral on the left-hand side of (3) is related to a numerical-flux integral on the right-hand side, which is enforced to be continuous across elements. A robust and efficient choice of the numerical flux is the so-called partially penalized flux [4], [9], [19]–[21], which has been proven to provide accurate and free of spurious mode solutions [22]

$$\begin{aligned} \hat{\mathbf{n}}^m \times \mathbf{E}^{m'} &= \hat{\mathbf{n}}^m \times \mathbf{E}^m + \chi_e^m [\hat{\mathbf{n}}^m \times (\mathbf{E}^{m+} - \mathbf{E}^m) + \mathbf{M}_s] \\ &\quad + \nu_h^m [\hat{\mathbf{n}}^m \times (\hat{\mathbf{n}}^m \times (\mathbf{H}^{m+} - \mathbf{H}^m) - \mathbf{J}_s)], \\ \hat{\mathbf{n}}^m \times \mathbf{H}^{m'} &= \hat{\mathbf{n}}^m \times \mathbf{E}^m + \chi_h^m [\hat{\mathbf{n}}^m \times (\mathbf{H}^{m+} - \mathbf{H}^m) - \mathbf{J}_s] \\ &\quad - \nu_e^m [\hat{\mathbf{n}}^m \times (\hat{\mathbf{n}}^m \times (\mathbf{E}^{m+} - \mathbf{E}^m) + \mathbf{M}_s)] \end{aligned} \quad (4)$$

with

$$k_e^m = \frac{Y^{m+}}{Y^m + Y^{m+}}, \quad k_h^m = \frac{Z^{m+}}{Z^m + Z^{m+}}, \quad (5)$$

$$\nu_h^m = \frac{\tau}{Y^m + Y^{m+}}, \quad \nu_e^m = \frac{\tau}{Z^m + Z^{m+}}, \quad (6)$$

where τ is a stabilization parameter that penalizes the discontinuities in the tangential components, $Z^m = \sqrt{\mu^m / \epsilon^m} = 1/Y^m$ the intrinsic impedance of the element m , and $Z^{m+} = 1/Y^{m+}$ the intrinsic impedance of the adjacent one. We have included in (4) possible surface currents required for the implementation of Huygen's sources [23] and used to excite the antenna feeding points.

Using a Faedo–Galerkin method

$$\mathbf{E}^m = \sum_{q=1}^Q e_q^m(t) \Phi_q^m(\mathbf{r}), \quad \mathbf{H}^m = \sum_{q=1}^Q h_q^m(t) \Phi_q^m(\mathbf{r}), \quad (7)$$

a final semidiscrete algorithm is found

$$\begin{aligned} \mu \mathbb{M} d_t H^m - \mathbb{F}_{vh} H^m + \mathbb{F}_{vh}^+ H^{m+} &= -(\mathbb{S} - \mathbb{F}_{xe}) E^m \\ &\quad - \mathbb{F}_{xe}^+ E^{m+} - M^{sx} + J^{sv} \end{aligned} \quad (8a)$$

$$\begin{aligned} \epsilon \mathbb{M} d_t E^m - \mathbb{F}_{ve} E^m + \mathbb{F}_{ve}^+ E^{m+} &= (\mathbb{S} - \mathbb{F}_{xh}) H^m \\ &\quad + \mathbb{F}_{xh}^+ H^{m+} - J^{sx} - M^{sv}, \end{aligned} \quad (8b)$$

where H^m and E^m are column vectors with the degrees of freedom (dofs); H^{m+} and E^{m+} are the dofs of the adjacent elements; M^{sx} , M^{sv} , J^{sx} , and J^{sv} are column vectors with the weak form

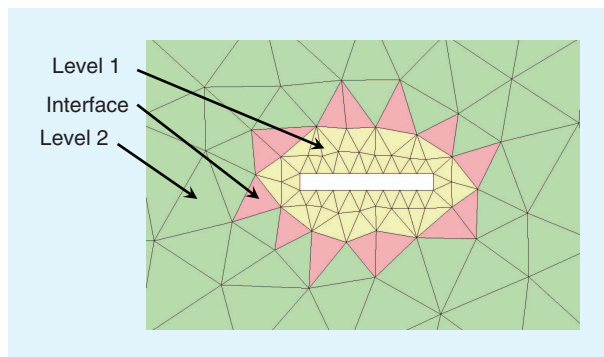


FIGURE 1. A 2-D classification example of two LTS levels and the interface.

of the surface source terms; \mathbb{M} is the mass; \mathbb{S} is the stiffness; and \mathbb{F} is the flux matrices given in [22].

For the TD integration, several approaches can be chosen. The most commonly employed ones are the RK4 [4] and the second-order LF [8] schemes. Both are conditionally stable and impose an upper bound on the maximum time step, which depends on each element characteristic: size, aspect ratio, and curvature (for quadratic elements), order of the local basis functions, material of adjacent elements, and boundary conditions on its faces [9]. The LF scheme selected in this article samples the unknown fields in a staggered way. Thus, the electric field is evaluated at $t_n = n\Delta t$ and the magnetic field at $t_{n+\frac{1}{2}} = (n+1/2)\Delta t$. In the same way, (8a) is evaluated at t_n and (8b) at $t_{n+\frac{1}{2}}$. The first-order time derivatives are approximated by a central difference ($d_t U_n \approx \Delta t^{-1} (U_{n+\frac{1}{2}} - U_{n-\frac{1}{2}})$) and the terms affected by the stabilization parameter by the backward approximation ($H_n^m \approx H_{n-\frac{1}{2}}^m$ and $E_{n+\frac{1}{2}}^m \approx E_n^m$) since an average would yield a globally implicit scheme due to the coupling terms from the adjacent elements [22], [24].

The resulting fully explicit LFDG algorithm is [22]

$$\begin{aligned} H_{n+\frac{1}{2}}^m &= H_{n-\frac{1}{2}}^m + \frac{\Delta t}{\mu} \mathbb{M}^{-1} [-(\mathbb{S} - \mathbb{F}_{ke}) E_n^m - \mathbb{F}_{ke}^+ E_n^{m+} \\ &\quad + \mathbb{F}_{vh} H_{n-\frac{1}{2}}^m - \mathbb{F}_{vh}^+ H_{n-\frac{1}{2}}^{m+} - M_n^{sk} + J_n^{sv}] \end{aligned} \quad (9a)$$

$$\begin{aligned} E_{n+1}^m &= E_n^m + \frac{\Delta t}{\epsilon} \mathbb{M}^{-1} [(\mathbb{S} - \mathbb{F}_{kh}) H_{n+\frac{1}{2}}^m + \mathbb{F}_{kh}^+ H_{n+\frac{1}{2}}^{m+} \\ &\quad + \mathbb{F}_{ve} E_n^m - \mathbb{F}_{ve}^+ E_n^{m+} - J_{n+\frac{1}{2}}^{sk} - M_{n+\frac{1}{2}}^{sv}]. \end{aligned} \quad (9b)$$

LTS ALGORITHM

A new LTS algorithm is proposed in this section. It is inspired by the recursive LF (R-LF) algorithm by Montseny et al. [9], with modifications to avoid the use of magnitudes at unknown times by others evaluated at different time instants, as detailed below. This algorithm starts by arranging the mesh elements into L levels. The time step for level l is $\Delta t_l = (2k+1)^{l-1} \Delta t_1$, with k being a positive real integer and Δt_1 the effective time step for the first level ($l=1$). All the elements of level l must fulfill the condition $\Delta t_l < \Delta t_{\text{MAX}}^m$ (where Δt_{MAX}^m is the maximum Δt for stability at the element m). For instance, $k=1$ means that there is a factor 3 between the time steps of consecutive levels.

At the preprocess stage, we classify all the mesh elements into $(2L-1)$ possible sets requiring a special treatment: L different levels plus the $(L-1)$ interfaces. Let us illustrate the procedure for simplicity for the two-dimensional (2-D) example shown in Figure 1, with two LTS levels ($L=2$). We first define two updating expressions, one for the electric field and the other for the magnetic field, from the LFDG algorithm of (9)

$$H_{n+\frac{p}{2}}^m = f_H(p\Delta t_1, H_{n-\frac{p}{2}}^m, H_{n-\frac{p}{2}}^{m+}, E_n^m, E_n^{m+}) \quad (10a)$$

$$E_{n+p}^m = f_E(p\Delta t_1, E_n^m, E_n^{m+}, H_{n+\frac{p}{2}}^m, H_{n+\frac{p}{2}}^{m+}), \quad (10b)$$

where p is an integer value that allows us to use the updating functions to compute samples of the fields at any multiple of Δt_1 .

The starting state for the full sequence is shown in Figure 2. The sequence of the proposed LTS algorithm based on (10) continues as follows (see also Figure 3).

- *Step 1.* Update the magnetic field, f_H , for level 1 ($H_{n+\frac{1}{2}}$), the interface, and level 2 ($H_{n+\frac{3}{2}}$). In the case of level 1, $p=1$ must be used, and for level 2 and the interface, $p=3$. All E_n needed are all available.
- *Step 2.* Update electric field, f_E , for level 1 and interface (E_{n+1}). In both cases, $p=1$ must be used. We need $H_{n+\frac{1}{2}}$; this information is available in level 1 but has to be evaluated in the interface by averaging $H_{n+\frac{3}{2}}$ and $H_{n-\frac{1}{2}}$, and in level 2 by interpolating $H_{n+\frac{1}{2}} = 2/3H_{n+\frac{3}{2}} + 1/3H_{n-\frac{3}{2}}$.
- *Step 3.* Update the magnetic field, f_H , for level 1 ($H_{n+\frac{3}{2}}$). Clearly, $p=1$ must be used. E_{n+1} is needed in level 1 and in the interface, both of which are available.
- *Step 4.* Update the electric field, f_E , for level 1 (E_{n+2}), interface, and level 2 (E_{n+3}). In the case of level 1, $p=1$ must be used, and for level 2 and the interface, $p=3$. We need $H_{n+\frac{3}{2}}$, which are available.
- *Step 5.* Update the magnetic field, f_H , for level 1 and for the interface ($H_{n+\frac{5}{2}}$). In both cases, $p=1$ must be used. We need E_{n+2} ; this information is available in level 1 but has to be evaluated in the interface by averaging E_{n+1} and E_{n+3} , and in level 2 by interpolating $E_{n+2} = 2/3E_{n+3} + 1/3E_n$.
- *Step 6.* Update electric field, f_E , for level 1 (E_{n+3}). Obviously, $p=1$ must be used. $H_{n+\frac{5}{2}}$ is needed, both in level 1 and in the interface, both of which are available.

This algorithm retains most of the advantages of the R-LF method (i.e., full explicitness and simplicity) but avoids the use of magnitudes at unknown times. Instead, they are calculated from the previous dofs, either by means of averages and interpolations or by the additional computation of certain states. The specific differences appear in Steps 2 and 5, where we make the averaging operation at the interface and compute the fields, thus requiring an interpolation on the upper level and also in Steps 3 and 6, where we use samples at known times since they have been computed in the previous steps. Note that the algorithm requires storing the electric and magnetic fields at two time levels around the level interfaces.

Concerning the stability of the scheme, as has been reported in [9] and [25], the stability condition must be strengthened in general. From our experience, we also need to apply a multiplicative factor of 0.8 to the estimated Δt_{MAX}^m of the non-LTS case, but only at the interface and its neighboring elements. This means that an extra stability condition is required for those elements. The algorithm has been tested in long and complex simulations in [22] and [24] without apparent instabilities. No additional dissipation (or spurious solutions) has been observed apart from that reported in [22].

The implementation of this scheme in a general multilevel ($L > 2$) case can be performed just by enforcing the interface elements of different levels not to be in contact. This is a minor requirement for practical meshes and avoids the use of a more restrictive multiplicative factor in the heuristic stability condition at the interfaces. It bears noting that the application of the

LTS will drive to highly refined meshes. It has been confirmed that the convergence of the spatial discretization of the fields is maintained in these cases [20].

ANTENNA FEEDING MODELS IN DG

The modeling of a coaxial port feed in DG can be carried out easily by making use of the flux terms, both for excitation and for absorption. For this, the first transverse electromagnetic (TEM) mode is injected into the coaxial port, in a weak manner through the flux terms, by introducing surface electric and magnetic current-density sources of the form

$$\mathbf{M}_s = \hat{\mathbf{n}}_p \times \mathbf{E}^{\text{inc}} \quad (11a)$$

$$\mathbf{J}_s = -\hat{\mathbf{n}}_p \times \mathbf{H}^{\text{inc}}, \quad (11b)$$

where $\hat{\mathbf{n}}_p$ is the unit vector normal to the port along the direction of propagation of the injected TEM mode. The incident fields are in cylindrical coordinates ρ and ϕ

$$\mathbf{E}^{\text{inc}} = V^{\text{inc}}(t) \frac{1}{\ln(b/a)} \frac{1}{\rho} \hat{\rho}, \quad (12a)$$

$$\mathbf{H}^{\text{inc}} = V^{\text{inc}}(t) \frac{1}{\eta \ln(b/a)} \frac{1}{\rho} \hat{\phi}, \quad (12b)$$

where a and b are the inner and outer radii of the concentric conductors, respectively, with the space between them filled with a dielectric of impedance $\eta = \sqrt{\mu/\epsilon}$. The time variation of the excitation signal is $V^{\text{inc}}(t)$.

The coaxial port, considered in single mode, is accurately truncated with a Silver–Müller impedance boundary condition, making it unnecessary to use perfectly matched layers (PMLs). In addition, the absorbing boundary condition can be located in the same surface as the port. The Silver–Müller condition is easily applied by using the following coefficients in the computation of the flux at the port surface:

$$k_e^m = k_h^m = \frac{1}{2}, \quad \nu_h^m = \frac{\eta}{2}, \quad \nu_e^m = \frac{1}{2\eta}. \quad (13)$$

Time	Level 1	Interface	Level 2
$(n-3/2)\Delta t_1$		H	H
$(n-1)\Delta t_1$	E		
$(n-1/2)\Delta t_1$		H	H
$(n)\Delta t_1$	E	E	E
$(n+1/2)\Delta t_1$			
$(n+1)\Delta t_1$			
$(n+3/2)\Delta t_1$			
$(n+2)\Delta t_1$			
$(n+5/2)\Delta t_1$			
$(n+3)\Delta t_1$			

FIGURE 2. The initial state of the electromagnetic fields for the three different sets of the scenario of Figure 1 ($L = 2$).

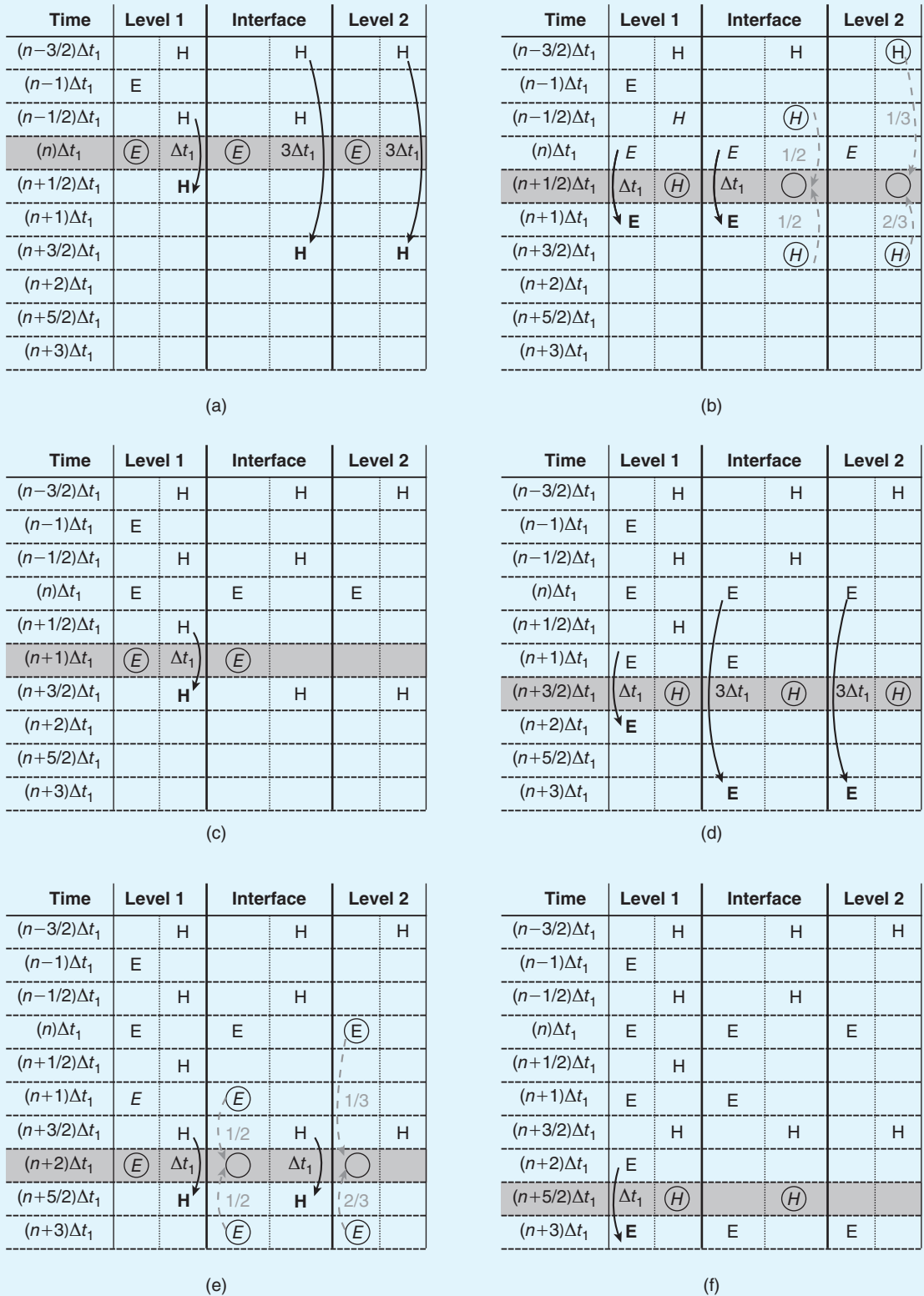


FIGURE 3. The sequence of the LTS algorithm for the scenario of Figure 1 ($L = 2$). The LF steps are drawn in solid lines and interpolation in dashed format. The required samples for an updating step appear inside a circle and the computed samples in bold. (a) Step 1. (b) Step 2. (c) Step 3. (d) Step 4. (e) Step 5. (f) Step 6.

We can evaluate the antenna impedance and the S_{11} parameter from the computation of the total voltage V^{tot} from the fields at the port surface. Notice that the space and time dependencies are separated in (12), and once the TEM mode is projected on the basis functions, all the source-term column vectors (M^{sk} , M^{sv} , J^{sk} , and J^{sv}) remain unchanged over the simulation, except for a time-dependent common factor depending on the time instant.

A simple alternative to the coaxial port is the well-known delta-gap feed model that is computationally less costly than the first one and can be accurate in some situations. Many implementations can be found in [26]. In this article, we chose to establish the given excitation voltage $V^{\text{inc}}(t)$ across the points of a surface gap [assumed to be a perfect electric conductor (PEC, commonly referred to as a hard source [26], [27]; a similar approach could be applied to the soft source)] through surface magnetic currents (coupled into the DG equations in the usual weak form). These are found from $\mathbf{E}^{\text{inc}} = V^{\text{inc}}(t)1/\Delta \hat{\mathbf{I}}_g$, where Δ is the gap width and $\hat{\mathbf{I}}_g$ is the unit vector following the gap orientation (see Figure 4), according to

$$\mathbf{M}_s = \hat{\mathbf{n}}_g \times \mathbf{E}^{\text{inc}} = V^{\text{inc}}(t) \frac{1}{\Delta} (\hat{\mathbf{n}}_g \times \hat{\mathbf{I}}_g), \quad (14)$$

where $\hat{\mathbf{n}}_g$ is the unit vector normal to the gap. Notice that the space and time dependencies are also separated in (14). The flux coefficients take the values

$$k_e^m = 1, \nu_e^m = \frac{\tau}{Z_m}, k_h^m = \nu_h^m = 0. \quad (15)$$

To evaluate the antenna impedance, we only need to compute the current flowing through the delta gap and divide it over the incident voltage.

To illustrate the differences between the two feeding techniques, we computed the input impedance and radiation patterns for some frequencies of a wideband conical antenna over an infinite ground plane, with the flare angle tuned for an asymptotic input impedance of $\sim 50 \Omega$. Figure 5(a) shows the setup and dimensions of the two simulated cases, excited by a coaxial port and a delta gap. Figure 5(b) compares both impedances (the impedance is not calculated at the same physical point since, between the radiating element and the coaxial port, there is a section of coaxial waveguide of 9.6 mm, which is not considered in the delta-gap case), showing differences along the entire band, while no significant differences are detectable in the radiation patterns [Figure 5(c)]. We can conclude that the simplified delta-gap model can be used as an alternative to the coaxial

one to predict the antenna radiation performance (in some cases, also its input impedance, e.g., if the antenna is fed by a matching network [28]), while a realistic model of the feeding should be employed for impedance prediction [26], [27] when the actual geometry of the port has a strong influence on the antenna behavior.

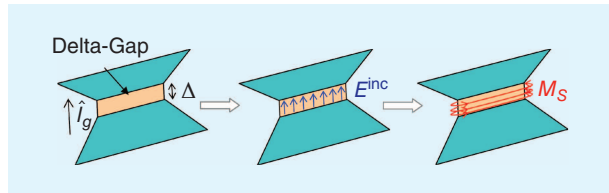


FIGURE 4. The delta-gap source model.

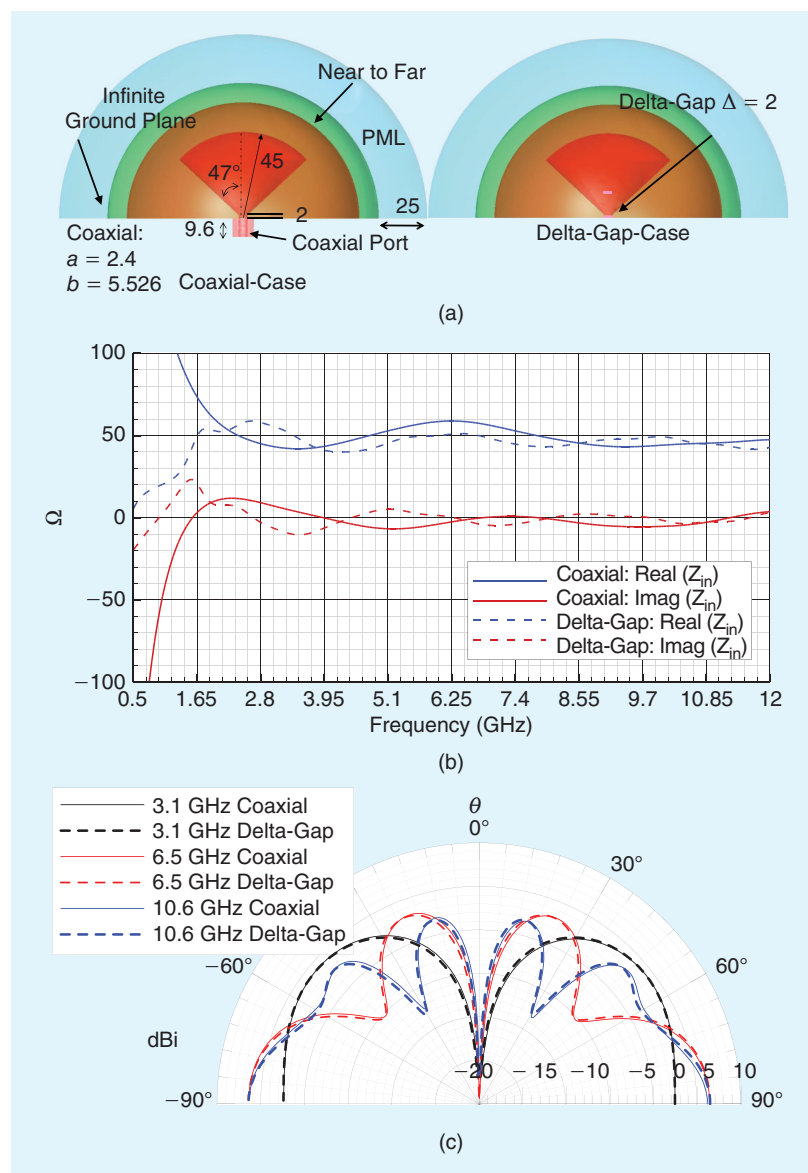


FIGURE 5. The conical antenna simulation case: (a) the simulation antenna setups with all dimensions in millimeters, (b) the input impedance results, and (c) the radiation pattern results.

APPLICATION

In this section, we illustrate the application of the LFDG to two cases: a typical biconical antenna (validated with measurements)

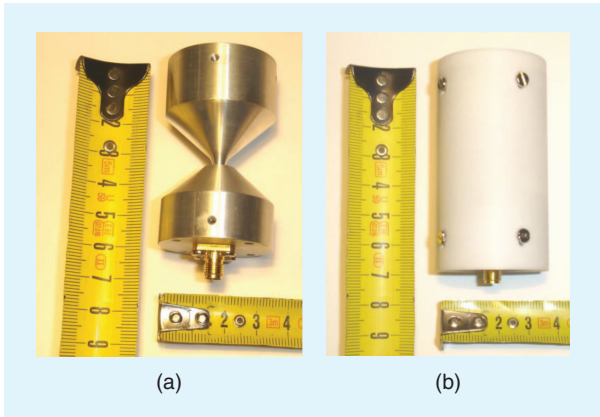


FIGURE 6. The wideband biconical antenna.

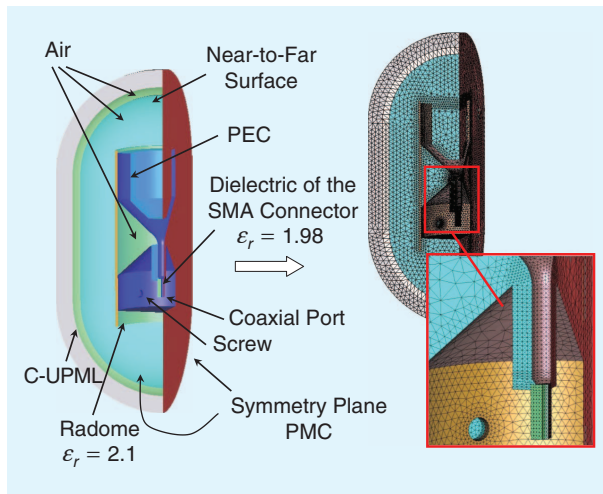


FIGURE 7. The simulation setup of the wideband bicone antenna. The antenna is fed through a subminiature version A (SMA) connector. PMC: perfect magnetic conductor.

and a monopole antenna integrated on a large structure (validated with the HFSS commercial package). In both cases, the high contrast in the elements' sizes makes the advantages of the LTS technique clear. The conformal uniaxial PML (C-UPML) [24], [29] is used to truncate the open free space.

BICONICAL ANTENNA

A biconical antenna was manufactured and measured to be used as a field sensor for low-level swept field (LLSF) measurements. The main objective of an LLSF test is to evaluate the transfer function between external and internal fields in a structure. This is a typical test in the aerospace electromagnetic compatibility sector to assess the shielding effectiveness inside the fuselage in the equipment bays. The key requirements for these antennas are small size, since they must fit inside any kind of cavity, and a wide frequency band. The biconical antenna shown in Figure 6 fulfills these requirements. It is formed by two cones connected by two sections of coaxial waveguides. Figure 7 shows the geometry and the simulation setup, where the high contrast of the elements' sizes in the mesh is evidenced. Figure 8 and Table 1 show the distribution of Δt_{MAX} with the elements and the different LTS levels for this simulation case.

The following aspects have been considered in the antenna modeling.

- The antenna is meshed with quadratically curved tetrahedrons. This is a key point because the geometry has revolution symmetry so that all the surfaces are curved (e.g., coaxial waveguide) and some of them doubly curved. Second-order finite elements significantly improve the spatial discretization and, consequently, the accuracy of the simulation.
- The order p of basis functions to expand the electric and magnetic field has been chosen depending on the element size to maintain uniform accuracy throughout the spatial domain with a reasonable amount of computational effort. We combined gradient spaces of reduced order $p - 1$ with rotational spaces of complete order p [30]. The numbers of elements and dofs per basis function set are shown in Table 2.

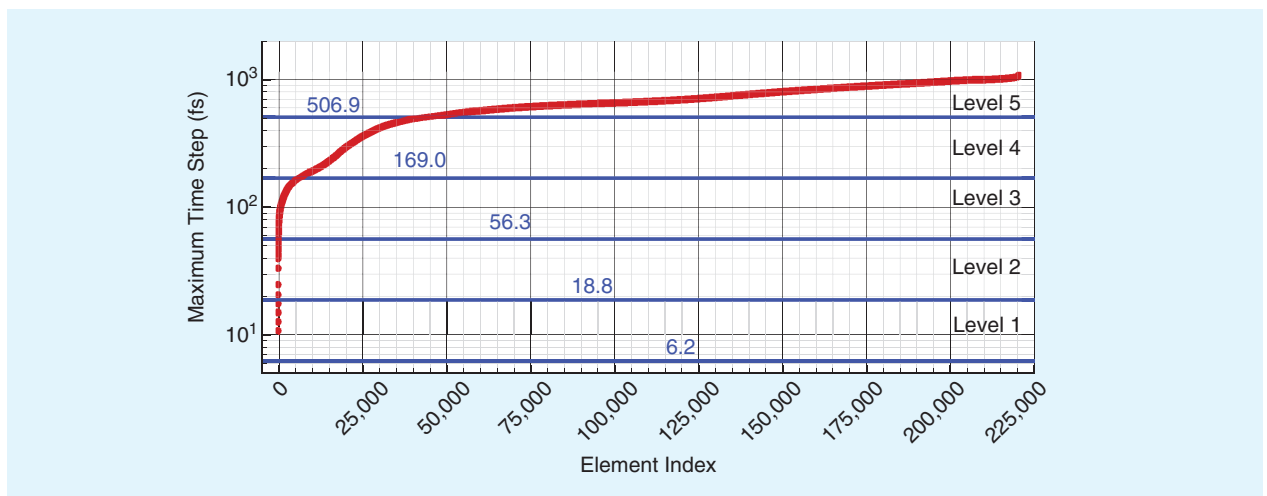


FIGURE 8. The distribution of the Δt_{MAX} with the elements.

TABLE 1. THE NUMBER OF ELEMENTS (M) IN EACH LTS LEVEL AND INTERFACE FOR THE BICONICAL SIMULATION CASE.

	L1	(L1/L2)	L2	(L2/L3)	L3	(L3/L4)	L4	(L4/L5)	L5
M	5	19	96	166	10,338	5,839	44,728	35,732	123,093
M (%)	0.002	0.01	0.04	0.08	4.7	2.65	20.33	16.24	55.95
Δt (fs)	6.2	18.8	18.8	56.3	56.3	169	169	506.9	506.9

- A conformal UPML [24], [29] technique has been used to truncate the computation space. This technique is shown to be reflectionless for any angle of incidence, polarization, and frequency. The conformity is used to reduce the buffer space and, thus, the time and memory requirements of each simulation.
- Due to the symmetry of the antenna, we have simulated one-quarter of the antenna, considering perfect magnetic conductor boundary conditions in the symmetry planes. This reduces the simulation times by a factor of four.

The coaxial port is excited with a Gaussian pulse time signal, with a 12-dB bandwidth at 20 GHz. The problem has been simulated until a physical time of 1.0 ns. Some screenshots of the simulation appear in Figure 9. The simulation time was 8.9 min for 20 AMD OPTERON dual-core 1.8-GHz processors. A reduction of 32 times in the

TABLE 2. THE NUMBER OF ELEMENTS (M) FOR EACH SET OF BASIS FUNCTIONS FOR THE BICONICAL SIMULATION CASE. GXRY STANDS FOR X ORDER FOR THE GRADIENT SPACE AND Y ORDER FOR THE CURL SPACE.

	G1R1	G1R2	G2R2	Total
M	177,933	41,906	177	220,016
M (%)	80.87	19.05	0.08	100
dofs	5,260,368	2,392,560	14,220	7,667,148
dofs (%)	68.61	31.21	0.18	100

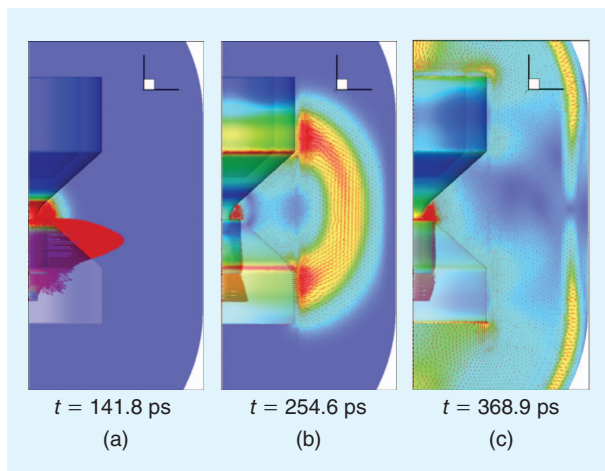


FIGURE 9. Screenshots of the simulation of the wideband biconical antenna.

central processing unit computational time is achieved by using the LTS algorithm compared with the time required without employing LTS.

The computed and measured S_{11} and input impedances are shown in Figure 10, where excellent agreement between them can be observed. The radiation patterns for different frequencies were evaluated and are shown in Figure 11.

ONBOARD ANTENNA MODELING

In the last example, we will use the LFDG method to analyze the effect on the radiation performance of an antenna designed

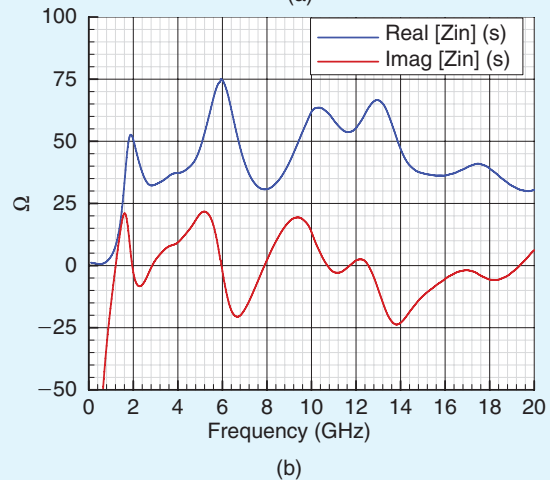
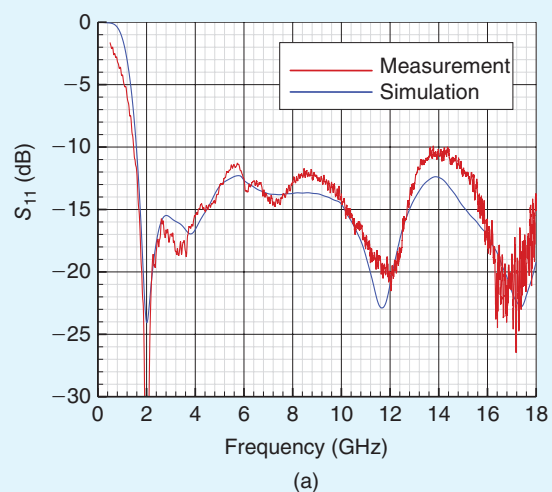


FIGURE 10. S_{11} and input impedance of the wideband biconical antenna. The measurement results of the S_{11} have been included for validation purposes.

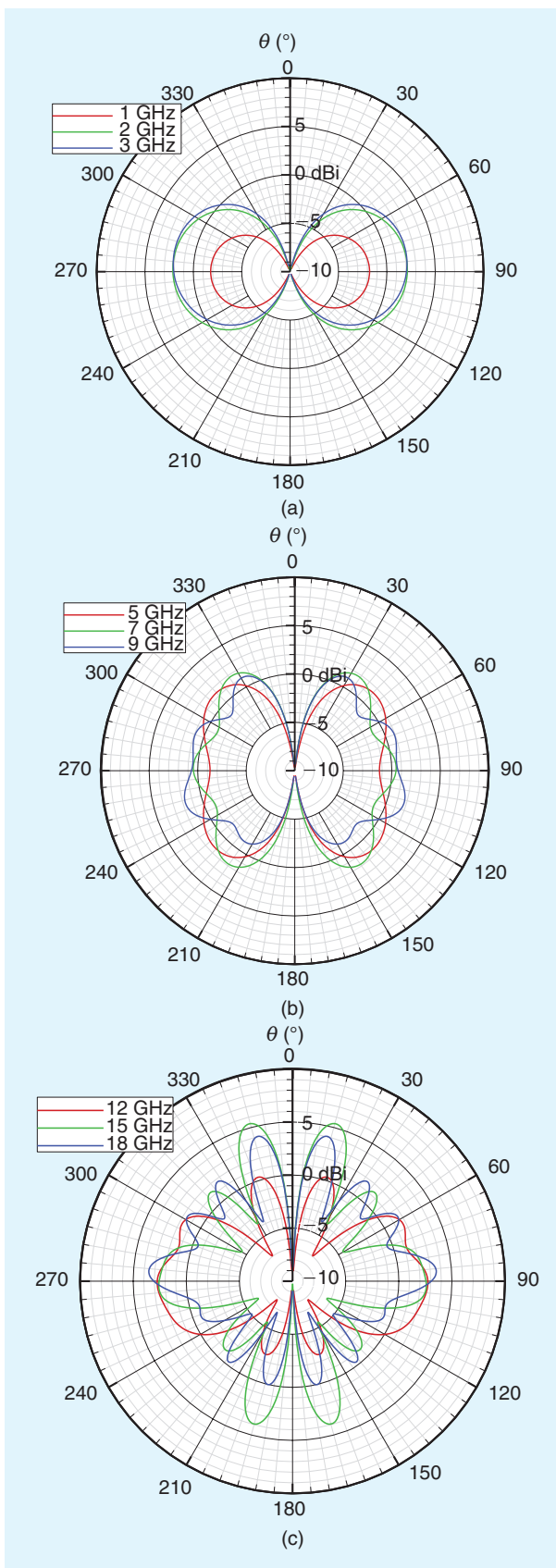


FIGURE 11. The radiation patterns of the wideband bicone antenna. The curves show the antenna gain for different frequencies in decibels-isotropic (dBi).

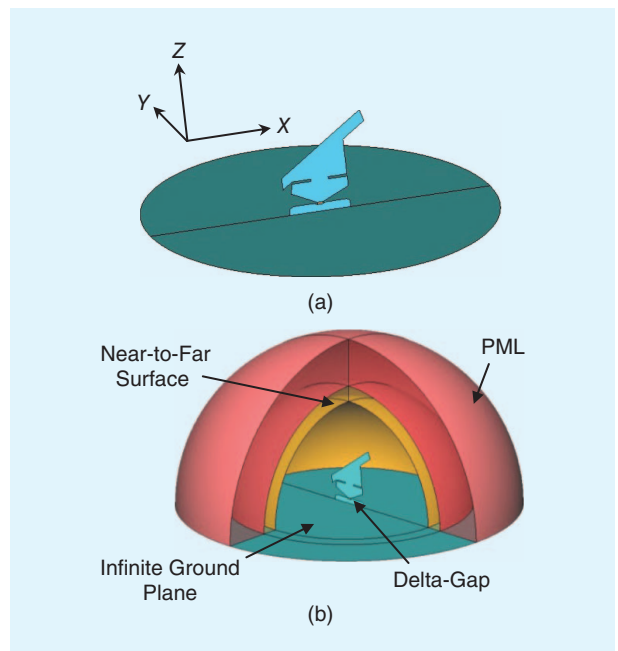


FIGURE 12. The antenna installed on an infinite ground plane.

to work in the very high-frequency (VHF) and ultrahigh-frequency (UHF) bands, installed in the leading edge of an aircraft fin, in comparison with its behavior with the antenna installed on an infinite ground plane (Figure 12), assuming a delta-gap model for the feeding. To keep the antenna size small, these onboard aircraft antennas are typically fed by a network matching. Figure 13 shows the radiation pattern of the ground-plane configuration. As expected, the loading structure on the top of the radiating element causes some energy to be radiated in the cross-polar component, which slightly reduces the antenna gain in the copolar component. This effect is more discernible in the UHF band.

The integration of this antenna in a leading edge of a generic aircraft fin is shown in Figure 14. As a preliminary approach, we simulated only a piece of the metallic tail [in blue in Figures 15(c) and 16(c)]. The antenna impedance and radiation patterns for two frequencies [132 MHz (VHF) and 312 MHz (UHF)] are shown in Figures 15–17. We find a relatively low degradation of the adaptation parameter compared with the infinite ground case. However, as expected, major differences due to the masking effect of the fin are found in the radiation patterns. For validation, we have included the impedance results in Figure 17 computed with the HFSS commercial software. A good agreement is found.

CONCLUSIONS

In this article, we have shown the applicability of an LTS-LFDG TD method to the accurate modeling of antenna structures. A new robust LTS strategy has been described in some detail, demonstrating its computational affordability. The classical delta-gap technique to model the antenna feeding has been revisited and compared with a more realistic coaxial equivalent model. Several realistic antennas used for

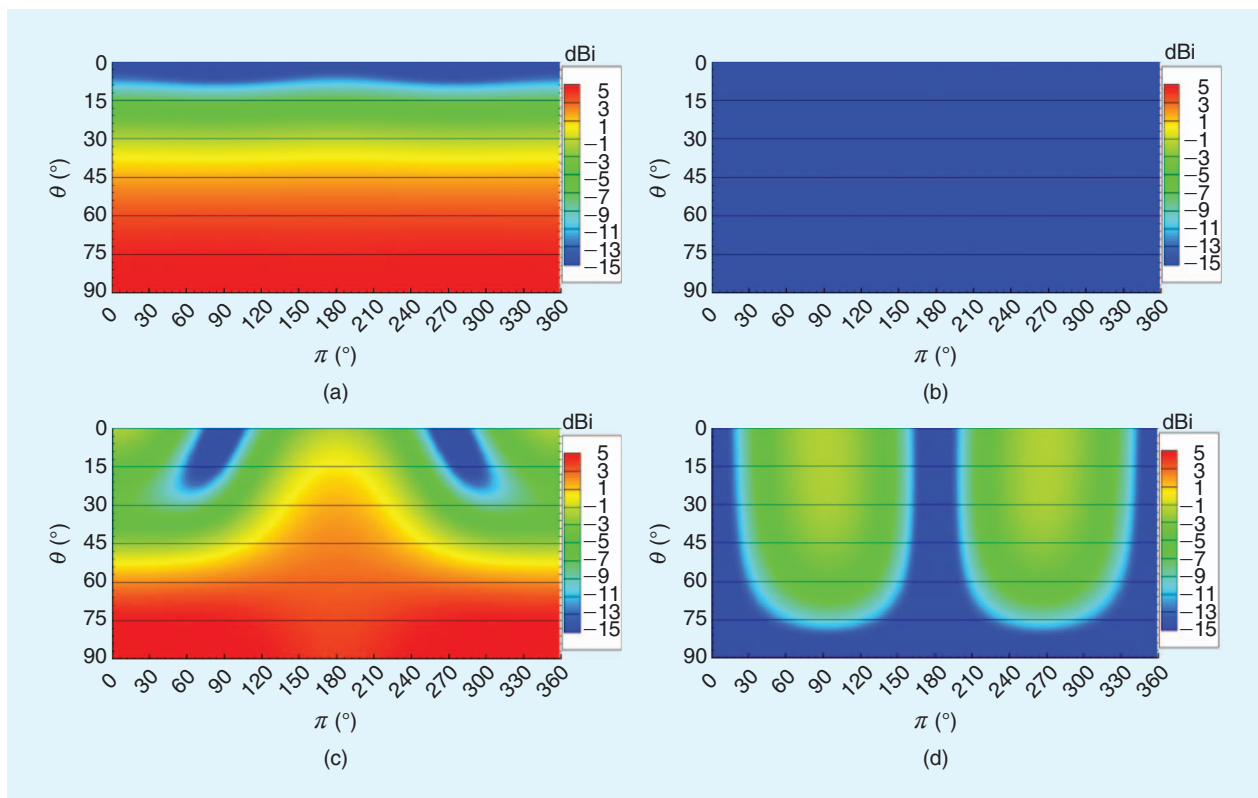


FIGURE 13. Theta versus pi radiation patterns with the antenna installed on an infinite ground plane.

aircraft testing or by onboard communication systems have been simulated to validate our approach by comparing them to measurements or HFSS results.

ACKNOWLEDGMENTS

We would like to thank Raul Molero Castejon from Cassidian and Pedro Garcia Morato from Airbus Military for the mounting and characterization of the wideband bicone antenna, which has made it possible for us to employ this geometry in our simulation and validation. The work described in this article is partially funded by the Spanish National Projects TEC2013-48414-C3-01, CSD2008-00068, P09-TIC-5327, and P12-TIC-1442 and by the GENIL Excellence Network.

AUTHOR INFORMATION

Jesus Alvarez (jesus@ieee.org) received his B.S. degree in 2001 from the University of Cantabria, Spain, his M.S. degree from the University Carlos III, Madrid, Spain, in 2008, and his Ph.D. degree from the University of Granada, Spain, in 2013. Since 2006, he has been with Airbus Defence and Space, working as an antenna and electromagnetic compatibility engineer. His current research interests include computational electrodynamics in the time domain, method of moments and fast algorithms for integral equations in the frequency domain, and computational electromagnetics applied to electromagnetic compatibility, antenna, and radar cross sections.

Luis Diaz Angulo (lm@diazangulo.com) received his B.S. and M.S. degrees in physics in 2005 and 2007, respectively, and his Ph.D. degree in 2014, all from the University of Granada,

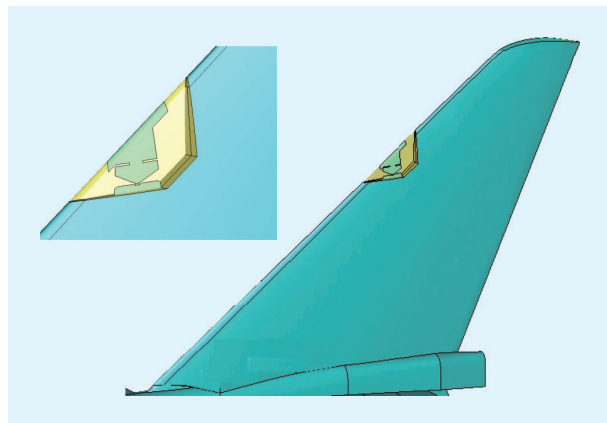


FIGURE 14. The antenna integration concept. The simulated part is shown in the upper left inset.

Spain. In 2015, he received his M.S. degree electronics engineering. He has worked in time-domain numerical methods applied to electromagnetism, especially discontinuous Galerkin time-domain methods. His other interests are applications of numerical methods in terahertz technologies, ground-penetrating radar (GPR) imaging, and bioelectromagnetics.

Amelia Rubio Bretones (arubio@ugr.es) received her Ph.D. degree in physics (cum laude) from the University of Granada, Spain, in 1988. Since 1985, she has been with the Department of Electromagnetism, University of Granada, first as an assistant professor, then in 1989 as an associate professor, and, since 2000, as a full professor. She has been a visiting

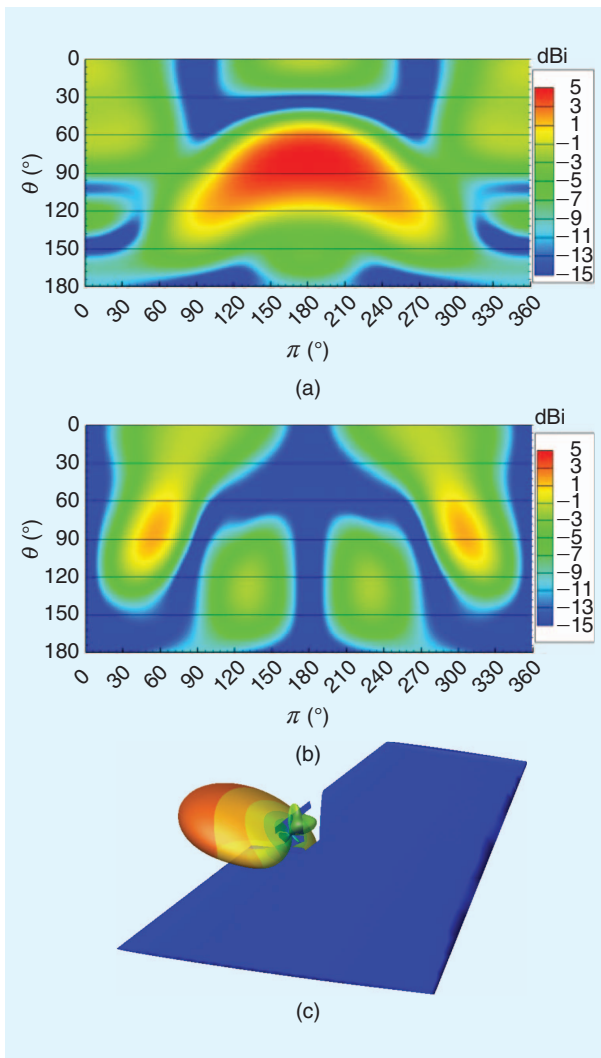


FIGURE 15. The radiation patterns for the antenna installed in the leading edge of the fin at 132 MHz. (a) Copolar. (b) Cross-polar. (c) Copolar three-dimensional (3-D) radiation pattern.

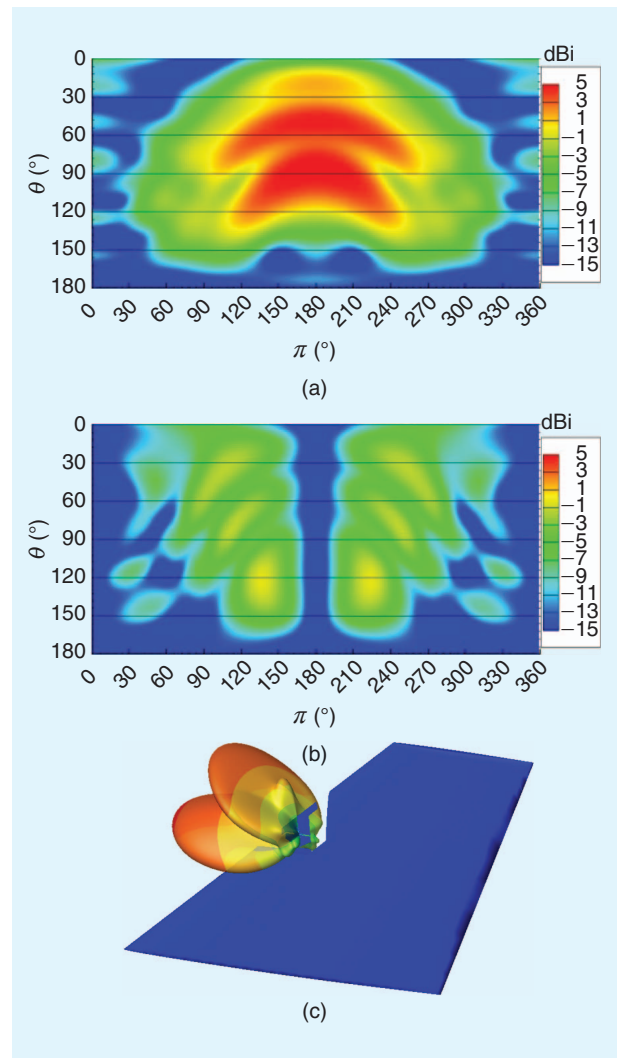


FIGURE 16. The radiation patterns for the antenna installed in the leading edge of the fin at 312 MHz. (a) Copolar. (b) Cross-polar. (c) Copolar 3-D radiation pattern.

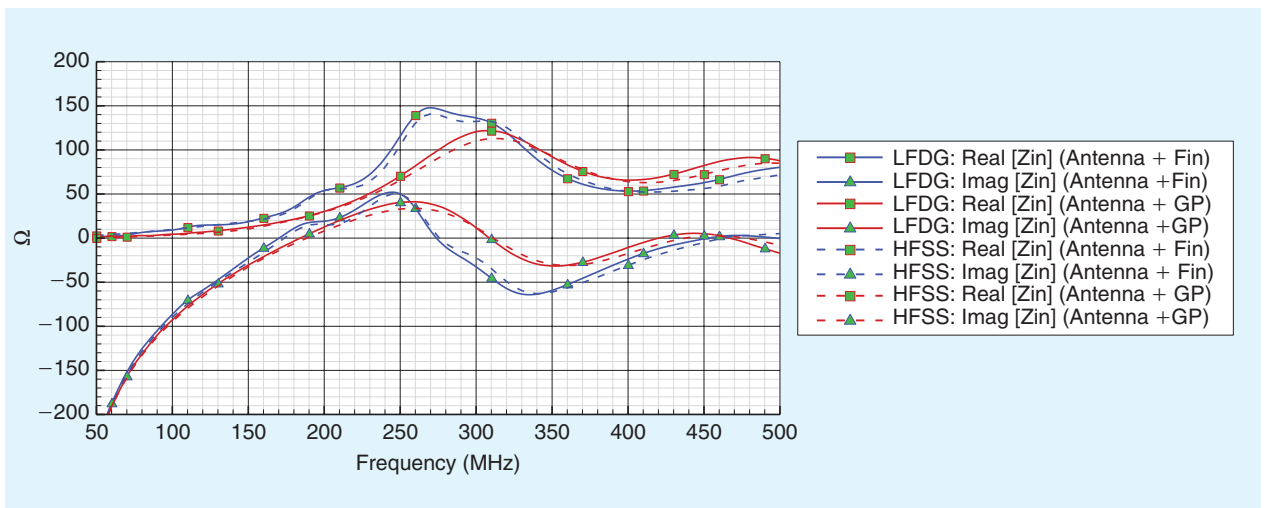


FIGURE 17. The input impedance with the antenna installed on the leading edge of the fin. The results of the antenna installed on an infinite ground plane have been included. The same computations have been performed with the HFSS commercial software.

scientist at the Delft University of Technology, the Eindhoven University of Technology, and Pennsylvania State University. Her research interest is mainly in the field of numerical techniques for applied electromagnetics, with an emphasis on time-domain techniques such as finite-difference time domain, the application of the method of moments in the time domain for antenna and scattering problems, and hybrid techniques.

Carlos M. de Jong van Coevorden (cmdejong@ugr.es) received his Ph.D. degree in physics (cum laude) from the University of Granada, Spain, in 2008. Since 2001, he has been with the electromagnetic group of Granada, within the Department of Electromagnetism, University of Granada, first as a research assistant in several national and international projects with public and private funding and, since 2009, as an assistant professor; he has qualified for associate professor since 2013. He has received grants to be a visiting scholar at the University of Pisa (2005), the University of Stellenbosch (2009 and 2010), and the University of Bello Horizonte. His current research interests include computational electromagnetics, radio-frequency (RF) design and measurements, application of optimization methods in RF engineering, and remote sensing.

Salvador G. Garcia (salva@ugr.es) received his M.S. and Ph.D. degrees (with honors) in physics from the University of Granada, Spain, in 1989 and 1994, respectively. In 1999, he joined the Department of Electromagnetism and Matter Physics, the University of Granada, as an assistant professor (and has been qualified for full professor since 2012). He has published over 50 refereed journal papers and book chapters and over 80 conference papers and technical reports, and he has participated in several national and international projects with public and private funding. He has received grants to be a visiting scholar at the University of Duisburg (1997), the Institute of Mobile and Satellite Communication Techniques (1998), the University of Wisconsin–Madison (2001), and the University of Kentucky (2005). His current research interests include computational electromagnetics, electromagnetic compatibility, terahertz technologies, microwave imaging and sensing (ground-penetrating radar), bioelectromagnetics, and antenna design.

REFERENCES

- [1] J. F. Lee, R. Lee, and A. Cangellaris, "Time-domain finite-element methods," *IEEE Trans. Antennas Propag.*, vol. 45, no. 3, pp. 430–442, Mar. 1997.
- [2] C. D. Sarris, *Adaptive Mesh Refinement in Time-Domain Numerical Electromagnetics*. San Rafael, CA: Morgan and Claypool Publishers, 2007.
- [3] S. Dey and R. Mittra, "A locally conformal finite-difference time-domain algorithm for modeling three-dimensional perfectly conducting objects," *IEEE Microwave Guided Wave Lett.*, vol. 7, no. 9, pp. 273–275, 1997.
- [4] J. S. Hesthaven and T. Warburton, *Nodal Discontinuous Galerkin Methods. Algorithms, Analysis, and Applications*. New York: Springer-Verlag, 2008.
- [5] H. Songoro, M. Vogel, and Z. Cendes, "Keeping time with Maxwell's equations," *J. Comput. Appl. Math.*, vol. 11, no. 2, pp. 42–49, Apr. 2010.
- [6] S. D. Gedney, C. Luo, J. A. Roden, R. D. Crawford, B. Guernsey, J. A. Miller, T. Kramer, and E. W. Lucas, "The discontinuous Galerkin finite-element time-domain method solution of Maxwell's equation," *J. Appl. Comput. Electromagn. Soc.*, vol. 24, no. 2, pp. 129–142, Apr. 2009.
- [7] H. Fu-Gang and W. Chao-Fu, "Higher-order DG-FETD modeling of wide-band antennas with resistive loading," *IEEE Trans. Antennas Propag.*, vol. 12, pp. 1025–1028, Aug. 2013.
- [8] L. Fezoui, S. Lanteri, S. Lohrengel, and S. Piperno, "Convergence and stability of a discontinuous Galerkin time-domain method for the 3D heterogeneous Maxwell equations on unstructured meshes," *ESAIM: Math. Model. Numer. Anal.*, vol. 39, no. 6, pp. 1149–1176, June 2005.
- [9] E. Montseny, S. Pernet, X. Ferrières, and G. Cohen, "Dissipative terms and local time-stepping improvements in a spatial high order discontinuous Galerkin scheme for the time-domain Maxwell's equations," *J. Comput. Phys.*, vol. 227, no. 14, pp. 6795–6820, 2008.
- [10] S. Piperno, "DGT methods using modal basis functions and symplectic local time-stepping: Application to wave propagation problems," *J. Comput. Phys.*, vol. 217, no. 2, pp. 340–363, Sept. 2006.
- [11] S. Piperno, "Symplectic local time-stepping in non-dissipative DGT methods applied to wave propagation problems," *ESAIM: Math. Model. Numer. Anal.*, vol. 40, no. 5, pp. 815–841, 2006.
- [12] G. Cohen, X. Ferrières, and S. Pernet, "A spatial high-order hexahedral discontinuous Galerkin method to solve Maxwell's equations in time domain," *J. Comput. Phys.*, vol. 217, no. 2, pp. 340–363, 2006.
- [13] F. Edelvik and G. Ledfelt, "A comparison of time-domain hybrid solvers for complex scattering problems," *Int. J. Numer. Model.: Electron. Networks, Devices Fields*, vol. 15, nos. 5–6, pp. 475–487, Sept.–Dec. 2002.
- [14] H. Fahs and S. Lanteri, "A high-order non-conforming discontinuous Galerkin method for time-domain electromagnetics," *J. Comput. Appl. Math.*, vol. 234, no. 4, pp. 1088–1096, 2010.
- [15] S. M. Schnepp and T. Weiland, "Efficient large scale electromagnetic simulations using dynamically adapted meshes with the discontinuous Galerkin method," *J. Comput. Appl. Math.*, vol. 236, no. 18, pp. 4909–4924, Dec. 2012.
- [16] J. J. W. van der Vegt and H. van der Ven, "Space-time discontinuous Galerkin finite element method with dynamic grid motion for inviscid compressible flows: I. General formulation," *J. Comput. Phys.*, vol. 182, no. 2, pp. 546–585, Nov. 2002.
- [17] P. Solin, L. Dubcova, and J. Kruijs, "Adaptive hp-FEM with dynamical meshes for transient heat and moisture transfer problems," *J. Comput. Appl. Math.*, vol. 233, no. 12, pp. 3103–3112, Apr. 2010.
- [18] S. M. Schnepp, "Error-driven dynamical hp-meshes with the Discontinuous Galerkin Method for three-dimensional wave propagation problems," *J. Comput. Appl. Math.*, vol. 270, pp. 353–368, Nov. 2014.
- [19] J. Alvarez, L. D. Angulo, A. R. Bretones, and S. G. Garcia, "3D discontinuous Galerkin time domain method for anisotropic materials," *IEEE Antennas Wireless Propag. Lett.*, vol. 11, pp. 1182–1185, Dec. 2012.
- [20] J. S. Hesthaven and T. Warburton, "High-order nodal discontinuous Galerkin methods for the Maxwell eigenvalue problem," *Philos. Trans.: Math. Phys. Eng. Sci.*, vol. 362, no. 1816, pp. 493–524, Mar. 2004.
- [21] R. Diehl, K. Busch, and J. Niegemann, "Comparison of low-storage Runge-Kutta schemes for discontinuous Galerkin time-domain simulations of Maxwell's equations," *J. Comput. Theor. Nanosci.*, vol. 7, pp. 1572–1580, 2010.
- [22] J. Alvarez, L. D. Angulo, A. R. Bretones, and S. G. Garcia, "A spurious-free discontinuous Galerkin time-domain method for the accurate modeling of microwave filters," *IEEE Trans. Microwave Theory Tech.*, vol. 60, no. 6, pp. 2359–2369, 2012.
- [23] J. Alvarez, L. D. Angulo, M. F. Pantoja, A. R. Bretones, and S. G. Garcia, "Source and boundary implementation in vector and scalar DGT," *IEEE Trans. Antennas Propag.*, vol. 58, no. 6, pp. 1997–2003, 2010.
- [24] J. Alvarez, L. D. Angulo, A. R. Bretones, M. R. Cabello, and S. G. Garcia, "A leap-frog discontinuous Galerkin time-domain method for HIRF assessment," *IEEE Trans. Electromagn. Compat.*, vol. 55, no. 6, pp. 1250–1259, 2013.
- [25] S. Dosopoulos and J. F. Lee, "Interior penalty discontinuous Galerkin finite element method for the time-dependent first order Maxwell's equations," *IEEE Trans. Antennas Propag.*, vol. 58, no. 12, pp. 192–197, Dec. 2010.
- [26] T. W. Hertel and G. S. Smith, "On the convergence of common FDTD feed models for antennas," *IEEE Trans. Antennas Propag.*, vol. 51, no. 8, pp. 1771–1779, Aug. 2003.
- [27] C. E. Brench and O. M. Ramahi, "Source selection criteria for FDTD models," in *Proc. IEEE Int. Symp. Electromagnetic Compatibility*, 1998, vol. 1, pp. 491–494.
- [28] Z. Lou and J. M. Jin, "Modeling and simulation of broad-band antennas using the time-domain finite element method," *IEEE Trans. Antennas Propag.*, vol. 53, no. 12, pp. 4099–4110, Dec. 2005.
- [29] T. Lu and P. Z. W. Cai, "Discontinuous Galerkin methods for dispersive and lossy Maxwell's equations and PML boundary conditions," *J. Comput. Phys.*, vol. 200, no. 2, pp. 549–580, Nov. 2004.
- [30] J. P. Webb, "Hierarchical vector basis functions of arbitrary order for triangular and tetrahedral finite elements," *IEEE Trans. Antennas Propag.*, vol. 47, no. 8, pp. 1244–1253, Aug. 1999.

